The Astrophysical Journal, 901:8 (7pp), 2020 September 20 https://doi.org/10.3847/1538-4357/abad3e
© 2020. The Author(s). Published by the American Astronomical Society.
OPEN ACCESS

Galactic Cosmic-Ray Hydrogen Spectra in the 40–250 MeV Range Measured by the High-energy Particle Detector (HEPD) on board the CSES-01 Satellite between 2018 and 2020

S. Bartocci[1], R. Battiston[2,3], W. J. Burger[2], D. Campana[4], L. Carfora[1,5], G. Castellini[6], L. Conti[1,7], A. Contin[8,9], C. De Donato[1], F. De Persio[1], C. De Santis[1], P. Diego[10], F. M. Follega[2,3], R. Iuppa[2,3], I. Lazzizzera[2,3], N. Marcelli[1,5], M. Martucci[1,5], G. Masciantonio[1], M. Mergé[1,14], G. Osteria[4], F. Palma[1,14], F. Palmonari[8,9], A. Parmentier[1], F. Perfetto[4], P. Picozza[1,5], M. Piersanti[1], M. Pozzato[9], I. Rashevskaya[3], E. Ricci[2,3], M. Ricci[11], S. Ricciarini[6], V. Scotti[4,12], A. Sotgiu[1], R. Sparvoli[1,5], P. Ubertini[10], V. Vitale[1], S. Zoffoli[13], and P. Zuccon[2,3]

[1] INFN, Sezione di Rome "Tor Vergata," I-00133 Rome, Italy; matteo.martucci@roma2.infn.it
[2] INFN—TIFPA, V. Sommarive 14, I-38123 Povo (Trento), Italy
[3] University of Trento, V. Sommarive 14, I-38123 Povo (Trento), Italy
[4] INFN—Sezione di Napoli, V. Cintia, I-80126, Naples, Italy
[5] University of Rome "Tor Vergata," Department of Physics, I-00133 Rome, Italy
[6] IFAC-CNR, V. Madonna del Piano, 10, I-50019 Sesto Fiorentino (Florence), Italy
[7] Uninettuno University, C.so V. Emanuele II, 39, I-00186, Rome, Italy
[8] University of Bologna, V.le Berti Pichat 6/2, Bologna, Italy
[9] INFN—Sezione di Bologna, V.le Berti Pichat 6/2, Bologna, Italy
[10] INAF-IAPS, V. Fosso Del Cavaliere 100, I-00133, Rome, Italy
[11] INFN—LNF, V.E. Fermi, 40, I-00044 Frascati (Rome), Italy
[12] University of Naples "Federico II"—V. Cintia, I-80126, Naples, Italy
[13] Italian Space Agency, V. del Politecnico, I-00133 Rome, Italy
Received 2020 July 16; revised 2020 August 5; accepted 2020 August 5; published 2020 September 16

Abstract

The High-energy Particle Detector (HEPD) on board the China Seismo-Electromagnetic Satellite (CSES-01)—launched on 2018 February 2—is a light and compact payload suitable for measuring electrons (3–100 MeV), protons (30–250 MeV), and light nuclei (up to a few hundreds of MeV). The Sun-synchronous orbit and large acceptance allow HEPD to measure cosmic-ray particles near the ±65° latitude limit for a fair amount of time per day. In this work, three semiannual galactic hydrogen energy spectra between ∼40 and 250 MeV are presented, including a comparison with theoretical spectra from HelMod, a 2D Monte Carlo model developed to simulate the solar modulation of cosmic rays throughout the heliosphere. To our knowledge, these are the first hydrogen energy spectra below 250 MeV measured at 1 au between 2018 and 2020.

Unified Astronomy Thesaurus concepts: Heliosphere (711); Cosmic rays (329); Cosmic ray detectors (325)

1. Introduction

Hydrogen nuclei (protons) are the most abundant components of charged galactic cosmic rays (CRs); they represent approximately 90% of the total CR budget and, together with helium nuclei, they account for ∼99% of the cosmic radiation. Evidence that the majority of CRs are accelerated in supernova remnants (SNRs) in the Galaxy are compelling, yet they are still inferred in an indirect way—see Baade & Zwicky (1934), Ginzburg & Syrovatsky (1961), Ackermann et al. (2013), Tavani et al. (2010), Giordano et al. (2012), Acciari et al. (2011), Berezhko & Völk (2007), and Vink (2012). From their site of production and acceleration, CRs propagate through the Galaxy interacting with the interstellar medium and diffusing on the permeating magnetic field before reaching the Earth's solar system (Amato & Blasi 2018). This ensemble of processes results in modifying the CR spectral shape with respect to the acceleration site. In the last decade, some experiments have provided evidence of peculiar features in CR proton and helium nuclei spectra at energies >200 GeV Panov et al. (2009), Adriani et al. (2011), Aguilar et al. (2015), and Yoon et al. (2017). At much lower energies (below a few GeV) the spectrum is bent downward because of the modulation effect exerted by the turbulent magnetized wind originated from the Sun. This heliospheric magnetic field (HMF) causes particle-field scattering and hinders very low energy particles from reaching the internal sectors of the solar system (inner Heliosphere). Such a phenomenon, called solar modulation, is the sum of a series of effects like convection, diffusion, adiabatic deceleration, and drift motions; this one related to the HMF curvatures and gradients (Potgieter 2013, 2017). CR modulation is time-dependent and it closely follows the 22 yr activity cycle of the Sun: higher fluxes are expected near minimum activity phases, while lower fluxes are expected during maximum phases. As an overall result, the energy spectrum of low energy charged cosmic particles is different with respect to the Local Interstellar Spectra (the spectra that would be measured outside the heliospheric boundaries) and its magnitude is strictly dependent on the period of the measurements (Cummings et al. 2016; Stone et al. 2019). The portion of the spectrum below a few hundreds of MeV is particularly interesting because the modulation effects are stronger, but also because solar transient phenomena such as SEPs (Bruno et al.

[14] Also at ASI Space Science Data Center (SSDC), V. del Politecnico, I-00133 Rome, Italy.

Original content from this work may be used under the terms of the Creative Commons Attribution 4.0 licence. Any further distribution of this work must maintain attribution to the author(s) and the title of the work, journal citation and DOI.

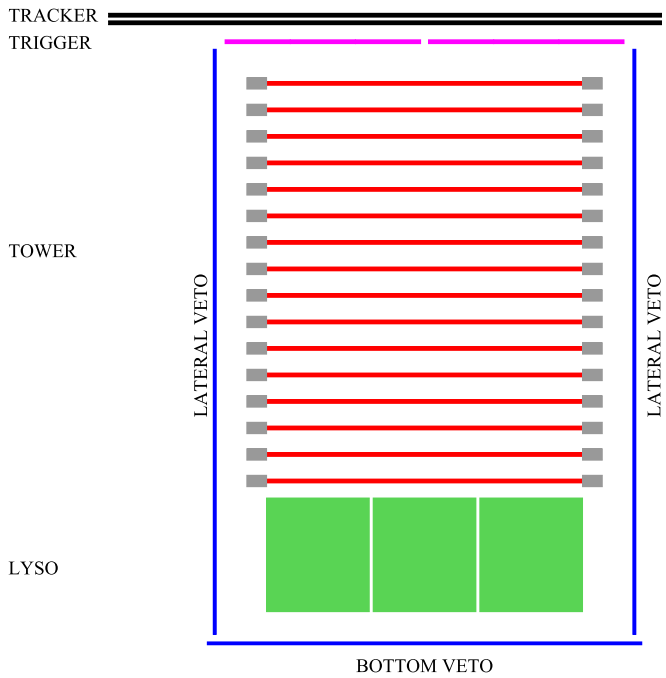

Figure 1. Schematic view of the HEPD apparatus: in the picture, the lateral veto plane located in the front has been removed for the purpose of visualization.

2018) and Forbush decreases (Munini et al. 2018) cause sudden injection and depletion that contribute to further modify the energy profile. Studies on modulated proton energy spectra below 200 MeV have been carried out mostly by balloons (Freier & Waddington 1968; Badhwar et al. 1967; Garrard et al. 1973) and, more recently, by the PAMELA experiment in both the 23rd (Adriani et al. 2013) and 24th solar cycles (Martucci et al. 2018).

In this work, we present three semiannual cosmic-ray hydrogen spectra measured by the High-energy Particle Detector (HEPD) in the ∼40–250 MeV range, during the period between the very end of the 24th solar cycle and the beginning of the 25th—from 2018 August to 2020 January.

2. The High-energy Particle Detector

The HEPD is a light and compact (40.36 cm × 53.00 cm × 38.15 cm, total mass ∼45 kg) payload designed and built by the Limadou Collaboration, the Italian branch of the CSES mission; a schematic view of the apparatus can be seen in Figure 1.

From top to bottom, the apparatus consists of a tracking system, including two 213.2 mm × 214.8 mm × 0.3 mm double-sided silicon microstrip planes, followed by a trigger system consisting of one EJ-200 plastic scintillator layer segmented into six paddles (20 cm × 3 cm × 0.5 cm each) and read out by two Photomultiplier Tubes (PMTs). The central portion of the instrument is occupied by a range calorimeter composed of two sections. The upper part, called TOWER, is a stack of 16 EJ-200 plastic scintillator planes (15 cm × 15 cm × 1 cm), each one read out by two PMTs. The lower part is a 3 × 3 matrix of LYSO (Lutetium–Yttrium Oxyorthosilicate) inorganic scintillator crystals, 5 cm × 5 cm × 4 cm each; each crystal is read out by a single PMT. Finally, an anticoincidence (VETO) system embeds the entire instrument and is composed of five EJ-200 plastic scintillator planes (0.5 cm thick), each one read out by two PMTs; four planes out of five surround the detector laterally, and one is placed below the LYSO matrix. The payload has a ±60° field of view and a geometrical acceptance of about 400 cm^2 sr @90 MeV for protons. A more detailed description of the instrument can be found in Ambrosi et al. (2018), Picozza et al. (2019), and Ambrosi et al. (2020).

HEPD was launched on board the China Seismo-Electromagnetic Satellite (CSES) on 2018 February 2 in the framework of a mission designed to investigate the top side of the ionosphere and to gather data on the near-Earth electromagnetic and particle environment with special focus on the lithosphere–atmosphere–ionosphere coupling. The satellite was put into a Sun-synchronous orbit, at ∼507 km altitude, 97° inclination and with a revisit time of ∼5 days. Due to attitude adjustments and other programmed maneuvers, HEPD (together with the other payloads on board CSES-01) is switched off below −65° and above +65°, but thanks to the large detector aperture, HEPD is able to collect galactic particles, though for a limited time per day. After a 6 month period of commissioning, HEPD started taking data, and a mission duration of >5 yr is foreseen. A deeper look at mission objectives and satellite characteristics can be found in Shen et al. (2018).

3. Data Analysis

3.1. Selection of Proton Events

In order to give a valid trigger to start data acquisition, a particle must cross a single paddle of the trigger plane (to avoid multiparticle events and reduce secondaries generated in the upper portion of the payload) and at least the first two planes of the upper calorimeter, P_1 and P_2. A paddle of the trigger, a plane of the upper calorimeter (TOWER) are considered hit if both PMTs (put in AND logic) collected an ADC signal above a certain threshold.[15] This signal is proportional to the deposited energy and the ADC-energy conversion is performed using results from beam test campaigns, see Ambrosi et al. (2020). The aforementioned thresholds are not fixed and, during the commissioning phase of the instrument, many of them were tested to choose the most suitable ones. After a valid trigger is acquired, only particles fully contained (namely, those that stop inside the TOWER+LYSO subdetector) are included in the flux sample; particles generating signals in one of the VETO planes are discarded. This is mandatory to guarantee that all the energy of the primary particle is deposited inside the instrument.

To discriminate between hydrogen nuclei and electrons/positron populations—HEPD is unable to distinguish particles with the same mass but opposite charge Z—a double-curve selection (each one of these curves has the form $y_i \propto \frac{A_i}{x}$ with A_i a constant) on the signal deposited on the first scintillator plane (P_1) as a function of the total deposited energy is required. The band, delimited by the aforementioned curves (quantiles at 15% and 95% for lower and upper curves, respectively), is large enough to collect ∼80% of the total hydrogen population and to reject as many high-energy leptons as possible. The P_1 signal distribution as a function of the total energy lost in the TOWER+LYSO subdetector is shown in Figure 2; the red curves represent the 15% and 95% quantile threshold used to

[15] For what concerns the LYSO matrix, the threshold check to define a hit in a crystal is applied to the single PMT reading each unit of this subdetector.

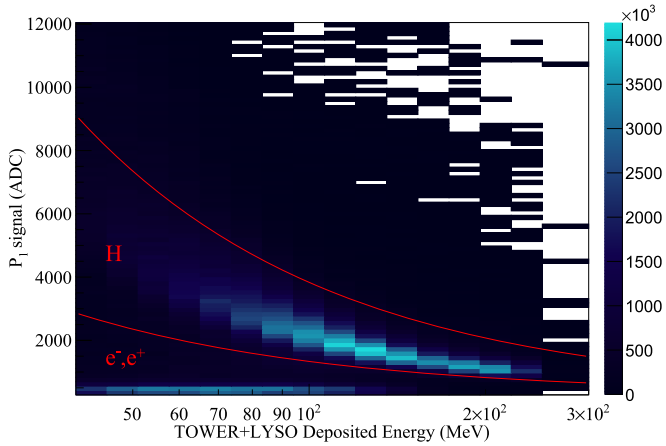

Figure 2. Hydrogen and electron/positron signals on plane P_1 as a function of the total energy deposited inside the calorimeter (TOWER+LYSO). To better visualize the separation in the plot, only vertical particles ($\theta < 15°$) have been selected. The red curves identify the selection used in this analysis to discriminate between hydrogen nuclei and the rest.

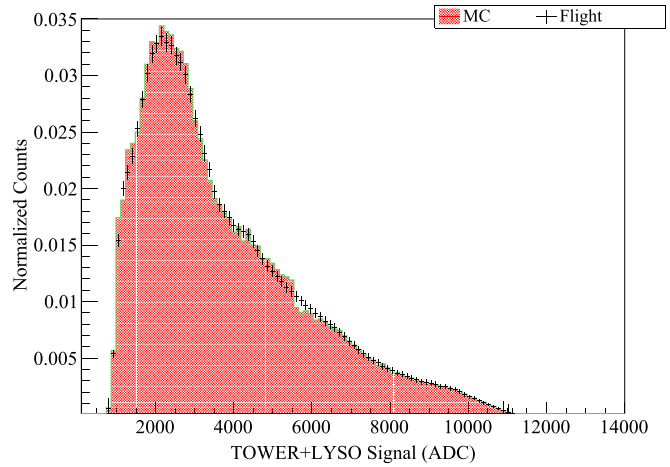

Figure 3. Comparison between proton total (TOWER+LYSO) ADC signal distribution obtained in flight (black markers) during the month of 2018 August and Monte Carlo simulation (red-shaded area).

select the hydrogen band. Auxiliary selections are applied to further clean the sample and to lower contamination. For example, if a particle is stopped at the ith plane, all the preceding $1...(i-1)$th planes must present a signal above threshold. Finally, a single LYSO crystal hit is required for energetic protons to avoid possible contamination from electromagnetic showers.

3.2. Geographical/Geomagnetic Selections

The highly inclined orbit of the CSES-01 satellite allows particles of various origins to be detected. To discriminate the primary (solar or galactic) component from the re-entrant albedo component (Adriani et al. 2015), it is necessary to evaluate the local rigidity cutoff (R) in each point of the orbit. Due to the large acceptance of HEPD, the Störmer approximation of vertical approaching particles (Shea et al. 1987) is no longer valid. A simulation on all possible arrival directions of protons has been carried out, considering the instrument field of view (FoV). A combination of the International Geomagnetic Field Reference (IGRF) model (Thébault et al. 2015), AACGM (Altitude-Adjusted Geomagnetic Coordinates; Shepherd 2014) and the Tsyganenko89 model (Tsyganenko 1989) is adopted to take into consideration both internal and external magnetic field sources. As a result, a latitude/longitude static cutoff map is obtained and employed as a template for the analysis. In the absence of major solar particle events and super-strong storms—except for the 2018 August 25–26 G3 geostorm that has been removed from the sample—a single map was used for all three periods (2018 August–2020 January). In order to remove the majority of electrons and re-entrant protons, we selected galactic particles in the geomagnetic region above 0.26 GV (∼35 MeV), such that all selected protons with energy >40 MeV were of galactic origin. This resulted in HEPD being able to detect cosmic protons for less than 10 minutes per day. This is a very strict, but also preliminary, approach; in the future, backtracing techniques will be adopted to better remove sub-cutoff particles even at lower latitudes, without affecting statistics. Throughout the analysis presented in this paper, the region of the SAA[16] was excluded to avoid saturation or pile-up issues that may occur under extremely high particle rates.

3.3. Live Time Evaluation

The live time $\tau_{\rm live}$ calculation of the apparatus is performed and managed via the trigger board. Moreover, both counters for the live and dead time ($\tau_{\rm live}$,$\tau_{\rm dead}$) are cross-checked with the on-board acquisition time of the DAQ board ($\tau_{\rm acquisition} = \tau_{\rm live}+\tau_{\rm dead}$). The related systematic is considered negligible with respect to the other sources of systematic errors. During the period 2018–2020, the trigger configuration (which affects the total acquisition time) was set to T & P_1 & P_2—see Section 3.1—which allows only particles crossing the trigger system and the first two planes of the upper calorimeter to be registered. For consistency with the geographical criteria introduced in Section 3.2, $\tau_{\rm live}$ is accumulated only in polar regions, where the rigidity cutoff is $0.26\,{\rm GV} < R < 0.35\,{\rm GV}$.

3.4. Geometrical Factor

The geometrical factor of HEPD is defined by the requirement of containment within the volume of the instrument: an incoming particle entering the upmost section of the payload, must be fully contained inside the calorimeter (TOWER+LYSO), see Section 3.1. It was evaluated using a Monte Carlo simulation of isotropically generated ($0° < \theta < 90°$ and $0° < \phi < 180°$) protons with primary energy ranging from 1 MeV to 10 GeV; such simulation was performed using the official software developed by the Limadou Collaboration, based on a GEANT4 toolkit Agostinelli et al. (2003). A careful digitization procedure, aimed to introduce instrumental ADC signal response in the simulation itself, was designed to reproduce and match the in-flight conditions. A comparison between the in-flight, fully contained proton ADC signal distribution and Monte Carlo is illustrated in Figure 3. The simulated protons must also fulfill the same series of auxiliary constraints described in Section 3.1 for in-flight protons. The total geometrical acceptance of HEPD for $Z = 1$ particles is shown in Figure 4; it presents a strong energy

[16] In our analysis, the South Atlantic Anomaly (SAA) region was defined as the area with magnetic field less than 26,000 nT.

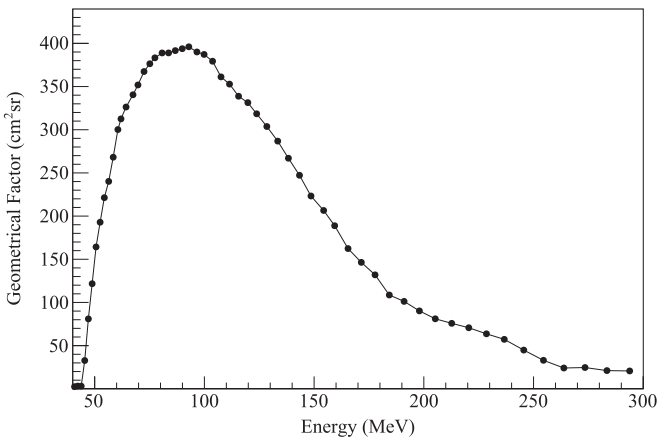

Figure 4. Total geometrical acceptance of HEPD for $Z = 1$ particles as a function of the energy. It shows a maximum value of $\sim$400 cm^2 sr @90 MeV, steeply decreasing at lower energies, because of the energy lost in hadronic interactions, and at higher energies, because of the narrower geometrical aperture.

dependence, with a value of $\sim$400 cm^2 sr @90 MeV, steeply decreasing at lower energies, because of the energy lost in hadronic interactions, and at higher energies, because of the narrower geometrical aperture. Various spectral shapes and energy ranges were used to cross-check the total acceptance as a function of the primary proton energy, and it was found constant within statistical errors.

3.5. Selection Efficiency

This includes both particle selection and instrumental efficiency. The former refers to the double-curve selection as a function of deposited energy, depicted in Figure 2. The resulting efficiency is $\sim$78%, almost constant between 40 and 250 MeV, and it was evaluated using the digitized Monte Carlo simulation already described in Section 3.4. The latter comprises all the instrumental inefficiencies that cannot be estimated by only using simulations, such as the variation in the response of sensitive components, aging processes and so on. These can be monitored, for example, comparing in-flight signal distributions to a reference period (the month of 2018 August was chosen because it was the first extended data-taking period after the commissioning phase of the satellite). A small variation (<5%) of the payload response was observed over the time 2018 August–2020 January and is taken into account as a systematic uncertainty.

3.6. Contamination

The major source of contamination for the low-energy hydrogen sample is given by >40 MeV electrons. Usually these MIP-like particles deposit a small amount of energy in the scintillators, being consequently rejected by the double-curve selection displayed in Figure 2; however, if they impinge the detector with an inclined trajectory, their energy release could be greater, thus contaminating the sample. The geomagnetic cut, described in Section 3.2, heavily reduces the amount of electrons contamination to $\sim$2% @40 MeV becoming slightly larger for energies >90 MeV where the lower proton selection curve possibly intersects the tail of the electron population. The presence of helium nuclei in the sample is negligible (due to the requested absence of signal deposited in the VETO planes that rejects the majority of heavier nuclei, which fragment inside the detector with consequent production of secondaries), while deuterium could not be separated from the hydrogen flux sample.

4. Statistical Deconvolution (Unfolding)

The proton energy spectrum measured in the entire calorimeter was corrected to account for particle slow-down and energy loss in the trigger paddles, tracker planes, and passive structures covering the sensitive materials of the apparatus. The correction, which is more relevant at low energies, has been applied by means of an unfolding procedure, following the classical Bayesian approach proposed in D'Agostini (1995, 2010). The detector response matrix, or smearing matrix, was obtained applying the same selections described in Sections 3.1 and 3.4 from a dedicated 1 MeV–10 GeV proton simulation, with a generic cosmic-ray spectrum (modulated power law) as an input. The unfolding procedure proved to be crucial to take into account the presence of >300 MeV protons that interact inside the detector, losing all their energy or generating undetectable neutrons that carry away a considerable fraction of the primary particle momentum, thus ending up mimicking a low-energy proton. The ADC signal distribution of such >300 MeV protons on P_1 is very similar to that of electrons, which cannot be effectively told apart from the former. From the simulation it was found that, for example, $\sim$1 GeV protons account for less than 5% of the total sample below $\sim$160 MeV, rising up to $\sim$15% between 160 and 250 MeV. After verifying that the instrument response remained unchanged within the 2 yr period under study—except for a small decrease in calorimeter overall efficiency—a single response matrix was employed for unfolding all three semiannual spectra.

5. Systematic Uncertainties

Possible sources of systematic uncertainties lie in both the deconvolution procedure and on the comparison between data and Monte Carlo. The former is related to the intrinsic accuracy of the adopted unfolding technique; it was estimated by folding and unfolding a known spectral shape with the response matrix. This systematic error as a function of energy is shown as red full circles in Figure 5. The latter includes the differences between flight data and Monte Carlo due to the digitization procedure and the limited statistics of the simulated proton sample. As already stated in Section 3.5, this uncertainty appears to be slightly time-dependent and the three systematics (one for every interval in which the energy spectrum was calculated) are shown in Figure 5 as black open circles, blue open squares, and green open triangles, respectively. The total systematic uncertainty is the squared sum of the single evaluated systematics.

6. Results

Three semiannual galactic hydrogen spectra as a function of energy between 40 and 250 MeV have been obtained in three different consecutive time periods (from 2018 August 6 to 2020 January 5) very much inside the heliosphere (1 au); the energy profiles are shown as black circles in Figure 6. Each measured energy spectrum is compared to the theoretical prediction from the HelMod model (Boschini et al. 2019) in the same period (blue solid curve); the maximum and minimum uncertainties related to this prediction are also reported in the

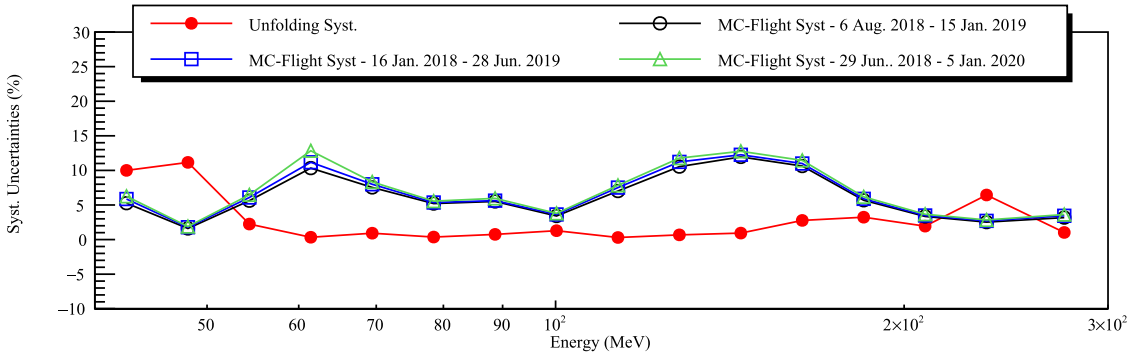

Figure 5. Various systematic uncertainties described in the text, as a function of energy: unfolding (red circles) and three Monte Carlo/flight systematic (black, blue, and green markers, respectively, for the three time intervals used in the analysis).

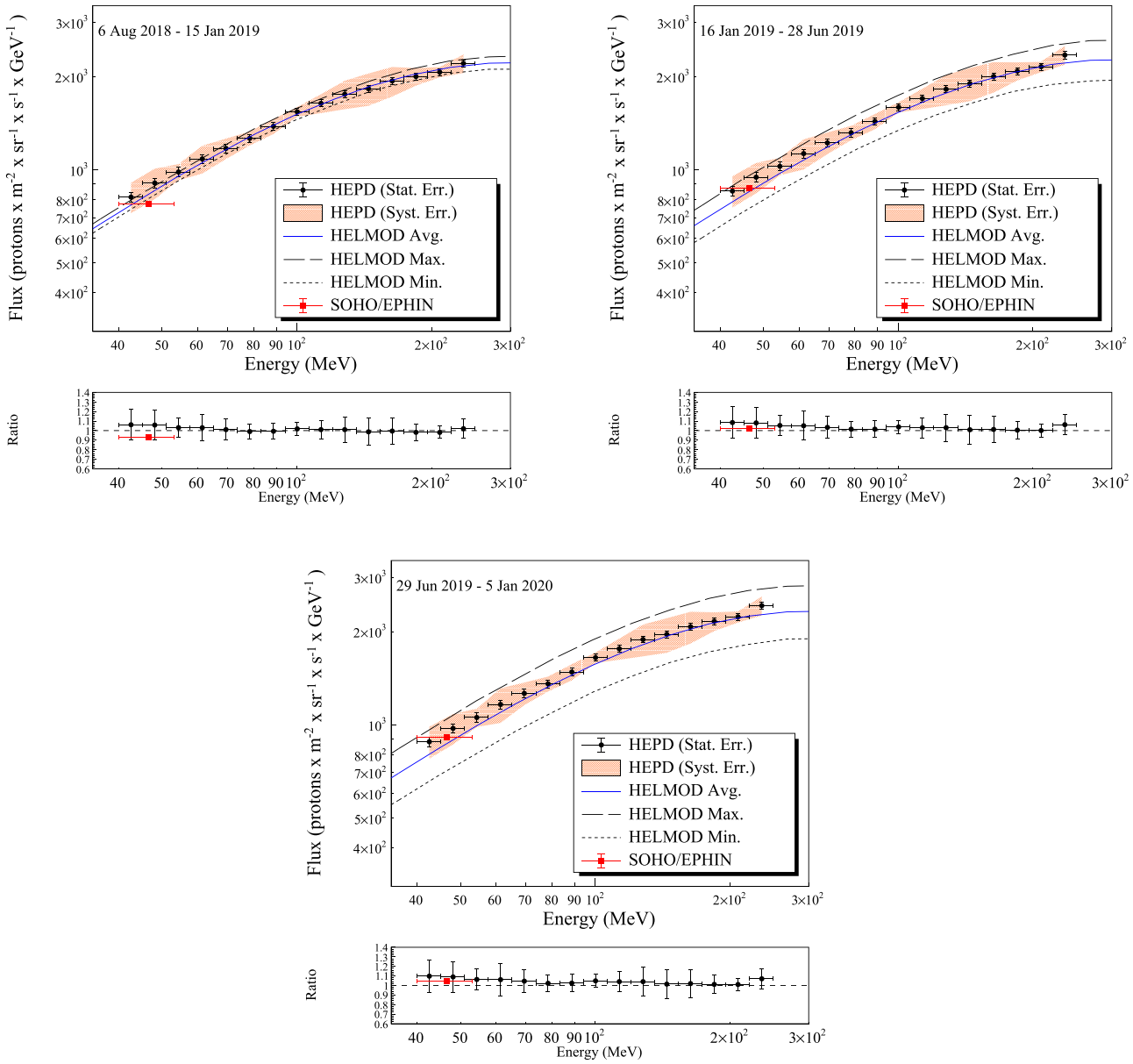

Figure 6. Large panel: galactic proton spectra as a function of energy measured by HEPD in the three intervals described in the text (from 2018 August 6 to 2019 January 15, from 2019 January 16 to 2019 June 28, and from 2019 June 29 to 2020 January 5, respectively). Systematic uncertainties are also present as a yellow shaded area. The continuous curves represent, respectively, the HelMod theoretical spectrum averaged over the period under study (blue solid line), the maximum (dashed line) and minimum (dotted line) expected deviation from the model itself. The red square represents data obtained from the SOHO/EPHIN spacecraft. Narrow panel: ratio between HEPD data and HelMod model, as a function of energy; errors on HEPD data are a sum of statistical and systematic uncertainties.

Table 1
Semiannual Hydrogen Galactic Proton Fluxes Measured by HEPD over the Three Time Periods Described in the Text; Both Statistical and Systematic Uncertainties Are Reported

Energy (MeV)	Flux (m^{-2} s^{-1} sr^{-1} GeV^{-1})		
	2018 Aug 6–2019 Jan 15	2019 Jan 16–2019 Jun 28	2019 Jun 29–2020 Jan 5
40.00–45.20	816.44 ± 30.34 ± 92.26	854.11 ± 31.39 ± 99.01	881.43 ± 32.11 ± 103.98
45.20–51.07	907.05 ± 33.13 ± 102.25	946.95 ± 34.31 ± 107.00	973.46 ± 34.35 ± 110.16
51.07–57.71	984.72 ± 34.16 ± 59.59	1027.16 ± 35.37 ± 66.61	1055.92 ± 35.38 ± 72.28
57.71–65.21	1085.42 ± 35.72 ± 112.21	1129.33 ± 36.90 ± 126.26	1163.68 ± 37.01 ± 149.51
65.21–73.68	1173.57 ± 36.81 ± 89.14	1223.02 ± 38.14 ± 98.44	1263.74 ± 38.36 ± 105.97
73.68–83.26	1265.50 ± 37.87 ± 66.06	1318.21 ± 39.28 ± 70.80	1356.75 ± 39.38 ± 75.55
83.26–94.07	1383.56 ± 39.73 ± 76.94	1434.89 ± 41.07 ± 81.49	1481.77 ± 41.30 ± 88.98
94.07–106.30	1541.60 ± 42.74 ± 56.19	1594.62 ± 44.07 ± 61.43	1649.37 ± 44.34 ± 66.06
106.30–120.11	1641.86 ± 44.15 ± 115.32	1702.34 ± 45.62 ± 128.04	1762.14 ± 45.89 ± 138.16
120.11–135.72	1757.32 ± 46.07 ± 185.77	1823.61 ± 47.66 ± 205.20	1888.11 ± 47.92 ± 222.76
135.72–153.36	1831.23 ± 47.24 ± 219.52	1902.62 ± 48.99 ± 233.94	1961.27 ± 48.94 ± 251.03
153.36–173.29	1939.96 ± 50.20 ± 213.15	2006.08 ± 51.83 ± 227.49	2076.55 ± 51.75 ± 244.63
173.29–195.81	2004.39 ± 52.17 ± 131.07	2087.06 ± 54.26 ± 140.24	2161.51 ± 53.84 ± 150.71
195.81–221.25	2071.98 ± 54.98 ± 80.15	2157.54 ± 57.18 ± 86.01	2234.50 ± 56.48 ± 92.62
221.25–250.00	2211.26 ± 61.67 ± 153.02	2352.90 ± 65.57 ± 164.43	2429.82 ± 64.78 ± 171.09

plots, as dashed and dotted lines, respectively. As a further comparison, data from the SOHO/EPHIN spacecraft (red square marker) between 40 MeV and 53 MeV are also presented (Müller-Mellin et al. 1995). The agreement appears to be good in all the three examined periods, considering both statistical and systematic uncertainties. Ratio between HEPD data and models (displayed in the narrower bottom panels of Figure 6) gradually worsens at lower energies, particularly below 65 MeV, where the spectrum calculated by HEPD is systematically higher. Possible explanations for this discrepancy include a contamination from high-energy protons that is not fully removed using the simulation, and a possible contamination derived from nuclei fragmentation or from very inclined sub-cutoff protons that can enter the FoV of the instrument, even after the rigidity cutoff selection. However, although systematic uncertainties are higher than 10% in the lowest portion of the energy spectra, these results could help constrain theoretical models of particle transport from the border of the heliosphere, down to 1 au. From a comparison between the first spectrum (2018 August 6–2019 January 15) and the last one (2019 June 29–2020 January 5) an overall increase of ∼9% is observed, in very good agreement with the variation observed in SOHO/EPHIN (∼8.5%). This behavior is expected, because, as the solar activity continues to wind down (from 2018 to 2020), the effect of the Sun magnetic field diminishes, resulting in higher proton fluxes. On the other hand, HEPD data do not show a clear energy dependence in the modulation over time (typically lower energies should be more modulated with respect to higher ones); unfortunately, for HEPD the overall errors (statistical and systematic) in the first and last energy bins do not allow such a precise evaluation. Table 1 contains explicit values for the galactic hydrogen spectra in the three time periods and for each of the 16 energy bins allowed by the instrument resolution; statistical and systematic uncertainties are also reported.

7. Conclusions

We have presented new results on the galactic hydrogen energy spectrum between 40 and 250 MeV obtained by the HEPD experiment during the period from 2018 August 6 to 2020 January 5, almost at the end of the 24th solar cycle. To our knowledge, these have been the first results on galactic hydrogen obtained in such an energy range, at 1 au, since a series of balloon flights in 1960s/1970s; the CSES-Limadou mission can be considered as an extension of PAMELA (2006–2016) in the study of low-energy cosmic rays. Moreover, another mission (CSES-02) is in preparation, and it is expected to offer further insight into low-energy physics throughout the 25th solar cycle.

This work makes use of data from the CSES mission (www.leos.ac.cn/) a project funded by China National Space Administration (CNSA), China Earthquake Administration (CEA) in collaboration with the Italian Space Agency (ASI), National Institute for Nuclear Physics (INFN), Institute for Applied Physics (IFAC-CNR) and Institute for Space Astrophysics and Planetology (INAF-IAPS). We kindly acknowledge both HelMod (http://www.helmod.org/) and OMNIWeb (https://omniweb.gsfc.nasa.gov/) websites for providing part of the data used in this paper. This work was supported by the Italian Space Agency in the framework of the "Accordo Attuativo" No. 2016-16-H0 Progetto Limadou Fase E/Scienza" (CUP F12F1600011005) and the ASI-INFN agreement n.2014-037-R.0, addendum 2014-037-R-1-2017.

ORCID iDs

S. Bartocci https://orcid.org/0000-0002-3066-8621
R. Battiston https://orcid.org/0000-0002-5808-7239
D. Campana https://orcid.org/0000-0003-1504-9707
L. Carfora https://orcid.org/0000-0002-2341-9870
G. Castellini https://orcid.org/0000-0002-0177-0643
L. Conti https://orcid.org/0000-0003-2966-2000
A. Contin https://orcid.org/0000-0002-2535-5700
C. De Donato https://orcid.org/0000-0002-9725-1281
F. De Persio https://orcid.org/0000-0003-4033-207X
C. De Santis https://orcid.org/0000-0002-7280-2446
P. Diego https://orcid.org/0000-0001-8279-020X
F. M. Follega https://orcid.org/0000-0003-2317-9560
R. Iuppa https://orcid.org/0000-0001-5038-2762
I. Lazzizzera https://orcid.org/0000-0001-5092-7531

N. Marcelli https://orcid.org/0000-0001-9375-735X
M. Martucci https://orcid.org/0000-0002-3033-4824
G. Masciantonio https://orcid.org/0000-0002-8911-1561
M. Mergé https://orcid.org/0000-0002-2018-4236
G. Osteria https://orcid.org/0000-0002-9871-8103
F. Palma https://orcid.org/0000-0001-7076-8830
F. Palmonari https://orcid.org/0000-0003-3707-0013
A. Parmentier https://orcid.org/0000-0002-9073-3288
F. Perfetto https://orcid.org/0000-0001-8119-5046
P. Picozza https://orcid.org/0000-0002-7986-3321
M. Piersanti https://orcid.org/0000-0001-5207-2944
M. Pozzato https://orcid.org/0000-0003-0279-5436
E. Ricci https://orcid.org/0000-0002-4222-9976
M. Ricci https://orcid.org/0000-0001-6816-4894
S. Ricciarini https://orcid.org/0000-0001-6176-3368
V. Scotti https://orcid.org/0000-0001-8868-3990
A. Sotgiu https://orcid.org/0000-0001-8835-2796
R. Sparvoli https://orcid.org/0000-0002-6314-6117
P. Ubertini https://orcid.org/0000-0003-0601-0261
V. Vitale https://orcid.org/0000-0001-8040-7852
P. Zuccon https://orcid.org/0000-0001-6132-754X

References

Acciari, V. A., Aliu, E., Arlen, T., et al. 2011, ApJL, 730, L20
Ackermann, M., Ajello, M., Allafort, A., et al. 2013, Sci, 339, 807
Adriani, O., Barbarino, G. C., Bazilevskaya, G. A., et al. 2011, Sci, 332, 69
Adriani, O., Barbarino, G. C., Bazilevskaya, G. A., et al. 2013, ApJ, 765, 91
Adriani, O., Barbarino, G. C., Bazilevskaya, G. A., et al. 2015, JGRA, 120, 3728
Agostinelli, S., Allison, J., Amako, K., et al. 2003, NIMPA, 506, 250
Aguilar, M., Aisa, D., Alpat, B., et al. 2015, PhRvL, 114, 171103
Amato, E., & Blasi, P. 2018, AdSpR, 62, 2731
Ambrosi, A., Bartocci, S., Basara, L., et al. 2018, ScChE, 61, 643
Ambrosi, G., Bartocci, S., Basara, L., et al. 2020, NIMPA, 974, 164170
Baade, W., & Zwicky, F. 1934, PhRv, 46, 76
Badhwar, G. D., Deney, C. L., Dennis, B. R., & Kaplon, M. F. 1967, PhRv, 163, 1327
Berezhko, E. G., & Völk, H. J. 2007, ApJL, 661, L175
Boschini, M. J., Della Torre, S., Gervasi, M., La Vacca, G., & Rancoita, P. G. 2019, AdSpR, 64, 2459
Bruno, A., Bazilevskaya, G. A., Boezio, M., et al. 2018, ApJ, 862, 97
Cummings, A. C., Stone, E. C., Heikkila, B. C., et al. 2016, ApJ, 831, 18
D'Agostini, G. 1995, NIMPA, 362, 487
D'Agostini, G. 2010, arXiv:1010.0632
Freier, P. S., & Waddington, C. J. 1968, JGR, 73, 4261
Garrard, T. L., Stone, E. C., & Vogt, R. E. 1973, Proc. ICRC (Denver), 2, 1336
Ginzburg, V. L., & Syrovatsky, S. I. 1961, PThPS, 20, 1
Giordano, F., Naumann-Godo, M., Ballet, J., et al. 2012, ApJL, 744, L2
Martucci, M., Munini, R., Boezio, M., et al. 2018, ApJL, 854, L2
Müller-Mellin, R., Kunow, H., Fleißner, V., et al. 1995, SoPh, 162, 483
Munini, R., Boezio, M., Bruno, A., et al. 2018, ApJ, 853, 76
Panov, A. D., Adams, J. H., Ahn, H. S., et al. 2009, BRASP, 73, 564
Picozza, P., Battiston, R., Ambrosi, G., et al. 2019, ApJS, 243, 16
Potgieter, M. 2017, AdSpR, 60, 848
Potgieter, M. S. 2013, SSRv, 176, 165
Shea, M. A., Smart, D. F., & Gentile, L. C. 1987, PEPI, 48, 200
Shen, X., Zhang, X., Yuan, S., et al. 2018, ScChE, 61, 634
Shepherd, S. G. 2014, JGRA, 119, 7501
Stone, E. C., Cummings, A. C., Heikkila, B. C., & Lal, N. 2019, NatAs, 3, 1013
Tavani, M., Giuliani, A., Chen, A. W., et al. 2010, ApJL, 710, L151
Thébault, E., Finlay, C. C., Beggan, C. D., et al. 2015, EP&S, 67, 79
Tsyganenko, N. A. 1989, P&SS, 37, 5
Vink, J. 2012, A&ARv, 20, 49
Yoon, Y. S., Anderson, T., Barrau, A., et al. 2017, ApJ, 839, 5